Systematic microRNA screening identifies miR-19b as regulator of temozolomide response through targeting PP2A serine-threonine phosphatase in glioblastoma.

Elham Kashani[1,2], Kristyna Hlavackova[1], Stefan Haemmig[1], Martin C Sadowski[1], Jaison Phour[1], Ulrich Baumgartner[1,3,4], Nicole Mueller-Wirth[1], Carmen Trefny[1], Bushra Sharf Den Abu Fakher[1], Coline Nydegger[1], Theoni Maragkou[1], Philippe Schucht[5], Pascal Zinn[6], Markus Lüdi[5], Thomas Michael Marti[7], Philippe Krebs[1], Erik Vassella[1*]

[1]Institute of Pathology, University of Bern, Bern, Switzerland
[2]Graduate School for Cellular and Biomedical Sciences, University of Bern, Bern, Switzerland
[3]Cell and Molecular Biology Department, QIMR Berghofer Medical Research Institute, Sid Faithfull Brain Cancer Laboratory, Brisbane, QLD, Australia.
[4]School of Biomedical Sciences, The University of Queensland, Brisbane, Australia
[5]Department of Neurosurgery, University Hospital Bern, Bern, Switzerland
[4]Department of Neurological Surgery, University of Pittsburgh School of Medicine, Pittsburgh, Pennsylvania, USA
[6]Department of Anesthesiology and Pain Medicine, University Hospital Bern, University of Bern, Switzerland
[7]Division of General Thoracic Surgery, Inselspital, Bern University Hospital, Bern, Switzerland
*Corresponding author: Prof. Dr. Erik Vassella
Institut für Pathologie, Murtenstrasse 31, 3010 Bern, Switzerland. Tel.0316329943/3238, Fax.0313818764. Email: erik.vassella@unibe.ch

Running title: miR-19b confers temozolomide resistance through PPP2R5E

Abstract

Despite standard of care, glioblastoma IDH wt (GBM) inevitably recur accentuating the need to elucidate mechanisms of therapy resistance. The DNA alkylating agent temozolomide (TMZ) triggers futile DNA mismatch repair cycles and persistent DNA double strand breaks, but tumors counteract this genotoxic stress by inducing DNA damage repair and survival pathways. GBM cells overexpressing miR-19b-3p were reproducibly selected by TMZ treatment in systematic lentiviral microRNA screens, a finding that was investigated mechanistically. Attenuation of miR-19b in glioblastoma

cell lines and primary glioblastoma stem cells (GSCs) induced DNA damage as indicated by enhanced CHK1 and CHK2 phosphorylation, γH2AX foci formation, and senescence. These phenotypes were further enhanced by TMZ treatment. Enhanced expression of miR-19b in GBM tissues was associated with downregulation of regulatory subunit PPP2R5E of Ser/Thr phosphatase PP2A in the mesenchymal subtype of GBM in agreement with miR-19b targeting PPP2R5E. Knocking down PPP2R5E antagonized the phenotypes elicited by miR-19b attenuation, and these effects were reversed in miR-19b attenuated/PPP2R5E knockdown cells suggesting a role of the miR-19b/PPP2R5E axis in TMZ-induced DNA damage response. In agreement with PP2A reactivation by miR-19b attenuation, PP2A activating drug, FTY720, or knocking down endogenous PP2A inhibiting proteins (PAIP), acted synergistically with TMZ to induce cell death. Enhanced TMZ resistance elicited by knocking down PPP2R5E was confirmed in orthotopic mouse GSC xenografts. These results provide insights in TMZ resistance mechanisms of GBM elicited by PPP2R5E targeting of miR-19b. Attenuation of miR-19b or PPP2R5E expression could potentially be exploited in adjuvant therapy of GBM.

Statement of significance

Systematic microRNA screening identified miR-19b implicated in temozolomide resistance through targeting PPP2R5E and interfering with DNA damage, senescence, and apoptosis in glioblastoma. This work provides insights into a new temozolomide resistance mechanism.

Keywords:

Glioblastoma; temozolomide resistance; miR-19b; PP2A; patient-derived xenograft

Introduction

Glioblastoma, IDH wt (GBM), the most common and most aggressive primary brain tumor in adults, remains an oncology challenge with a discouraging median two-year survival rate of 3.3% (1). The current standard of care for patients diagnosed with GBM is a combination therapy regimen of surgical resection, DNA alkylating agent therapy with temozolomide (TMZ) and radiation therapy (RT). Administration of TMZ results in cytotoxic O^6-methylguanine (O^6-MeG), N^7-methylguanine and N^3-methyladenine DNA adducts (2), which if remained unrepaired may lead to senescence and apoptosis. O^6-MeG alkylation can be repaired in a single step reaction mediated by O^6-MeG DNA methyl transferase (MGMT), leading to poor TMZ response. However, in 45% of GBM patients, MGMT is silenced by promoter hypermethylation which is associated with a better therapy response (3). If remained unrepaired, O^6-MeG mispairs with thymine causing futile cycles of mismatch repair (MMR), and one-ended DNA double stranded breaks (DSBs) occur owing to collapsed replication forks during the next round of replication. DSBs are primarily repaired by homologous recombination (HR) and, to a lower extent, also by error-prone non-homologous end joining (4). DSBs recruit the Mre11-Rad50-Nbs1 sensor complex to the damaged site. Ataxia telangiectasia mutated (ATM) and ataxia telangiectasia Rad3-related (ATR) are activated, initiating a cascade of downstream effectors including H2AX, 53BP1 and checkpoint kinases Chk1 and Chk2 resulting in cell cycle arrest mainly in G2/M and DNA repair.

Acquired resistance to TMZ may be due to increased expression of MGMT (5) or acquisition of loss of function mutations, underexpression or inhibition of mismatch repair genes (6). This may result in more efficient removal of O^6-MeG adducts, reduced mispairing with thymine and hence reduced DSBs in a fraction of recurrent GBM.

Enhanced HR activity (4) due to overexpression of ROCK2 (7) may be an alternative mechanism of acquired TMZ resistance. Activation of anti-apoptotic pathways, autophagy and senescence are additional survival strategies of GBM cells to cope with these cytotoxic effects (2). Longitudinal analyses of recurrent GBM was performed with the aim to elucidate TMZ resistance mechanisms of GBM (8,9). However, there was no evidence for persistent secondary alterations driving tumor recurrence. Instead, high plasticity was the major cause of tumor recurrence.

MicroRNAs (miRNA) are key post-transcriptional regulators of gene expression that are also involved in DNA repair pathways (for review see (10)) pursuing a fine-tuning of repair and also contribute to TMZ resistance processes. However, their role in TMZ resistance has not been systematically analyzed.

Here, we performed unbiased systematic screens for microRNAs conferring TMZ resistance using a pooled lentiviral miRNA library and reproducibly identified miR-19b overexpressing clones. We show that miR-19b targets PPP2R5E regulatory subunit of serine/threonine phosphatase PP2A and provide a new mechanism by which miR-19b controls TMZ response of GBM.

Material and methods

GBM patient cohort(s)

Two retrospective GBM cohorts, the microRNA screen discovery cohort (n=28) consisting of therapy-naive IDH wt GBM (11) and the longitudinal cohort (n=43) consisting of matched initial (therapy-naïve) and recurrent tumors with an interval of at least one year between pre-therapeutic and post-therapeutic resections, and 10 normal adjacent brain tissue (9) were used in this study. All patient samples were approved by the Cantonal Ethics Commission of the Canton of Bern (KEK-BE:2018-00663), which waived the requirement for written informed consent.

Cell lines and primary cells

Human primary Glioblastoma stem cells GSC3 and GSC4 were collected intraoperatively from patients with GBM IDH wt at MD Anderson (12). GSCs were cultured in GSC media (DMEM/F12 containing 1× B27, 20 ng/ml, EGF and 20 ng/ml basic fibroblast growth factor). The mutational profile of GSCs was assessed using the Trusight oncology 500 cancer panel (Illumina) and a Novaseq 6000 instrument. Identified mutations are shown in suppl. Table 1.

U87MG (kindly provided by M.E Hegi (University of Lausanne)), T98G and LN229 (purchased from American Type Culture Collection) were cultured with 10% fetal bovine serum (Sigma) at 37°C and 5% CO_2 (11) at maximally 70% confluence. Cells were genotyped and authenticated by Microsynth (Switzerland) and tested negative for mycoplasma infection. If not otherwise stated, cells were treated with 100µM TMZ.

Patient-derive xenograft (PDX) mouse model

Forty 6-week-old nude (athymic (Crl:NU(NCr)-Foxl nu) mice (Charles River) were anesthetized by subcutaneous injection with a mixture of fentanyl (0.05 mg/kg), midazolam (5 mg/kg) and medetomidine (0.5mg/kg) and injected orthotopically into the right forebrain with 1-2x10^5 GSC4 in 5µl medium. All animals were treated with a dosage of 66mg/kg TMZ by oral gavage daily for five consecutive days starting two weeks after injection, then rested for 3 weeks. This procedure was repeated twice (total 3 cycles). GSC4 cells were transduced with a beetle luciferase reporter construct (13). For monitoring tumor size by bioluminescence, mice were injected subcutaneously with luciferase substrate solution (VivoGlo Luciferin, In Vivo Grade (Promega #P1041) at a concentration of 150mg/kg bodyweight in 10µl/g bodyweight and the tumor size was analyzed using an in vivo imaging system (IVIS) instrument. Animal experiments were authorized by the veterinary office of the Kanton Bern (BE68/2021). According to

the approved animal score sheet, mice were euthanized at the earliest onset of neurological symptoms, or severe weight loss. Euthanizing and tumor-related death were considered as death events for Kaplan-Meier analysis.

Constructs and transfection

Luciferase reporter plasmids were constructed using the pmiRGLO Dual-Luciferase miRNA Target Expression Vector (Promega, Dübendorf, Switzerland) (14). Generation of lentiviruses and lentiviral transduction of GBM cell lines were performed as described (14). Transient transfection of short RNAs was performed as described (11). Sequences of oligonucleotides and lentiviral constructs used in this study are indicated in suppl.Table2.

MicroRNA lentivirus screen and NGS

$2.5x10^6$ IFU/ml of pooled lenti-microRNA lentivirus library (System Biosciences Cat. #PMIRHPLVHT-1) was mixed with 4mg/mL polybrene (Sigma) and transduced into $5x10^5$ cells at a MOI of 0.3-0.4 to ensure single lenti-miR integration. Three days post-transduction, cells were treated with 1.5µg/ml puromycin for three days and subsequently treated with TMZ. Selection was started with 25µM TMZ, and increased to 100µM.

For NGS analysis, lentiviral fragments encompassing the pri-miRNA sequence were amplified by PCR using the High-Fidelity MasterMix (NEB) and 400ng genomic DNA, 0.5µM primers and 1mM $MgCl_2$ for 30x cycles. DNA fragmentation was performed using the Next Fast DNA Fragmentation & Library Prep Set (NEB). 100ng purified DNA library was ligated with 2µl barcode and 2µl P1 (ThermoFisher). NGS analysis was performed using an Ion Torrent PGM (ThermoFisher). Differential expression analysis was performed using the RNA Sequencing Data Analysis Workflow from CLC Genomics Workbench (Qiagen). Relative coverage was calculated to the total reads.

Fragment size distribution during TMZ selection was assessed by PCR using FAM-labeled reverse primer. Fragment size distribution was assessed using a GA3500 genetic analyzer (ThermoFisher).

RNA analysis

RNA extraction and RTqPCR was performed as described (14). Primers used for qPCR are shown in suppl.Table1.

Microarray gene expression profiling using Nanostring cancer progression custom panel and bioinformatic analysis was performed as described (9).

Cell based assays

Luciferase reporter assays, cell viability assays using alamarBlue and Resazurin, caspase3/7 activity using the ApoTox-Glo Triplex kit (Promega), BrdU incorporation assay, colony formation assay and wound healing assay were performed essentially as described (14). For colony formation assay cells were treated with 15-30μm TMZ for 2 weeks initiating 16h post-seeding.

For β-galatosidase (SA-β-gal) staining assay, $3x10^4$ cells were seeded in 6-well plates and treated with 25μM or 50μM TMZ for 48h initiating 16h post-seeding. SA-β-gal assay was performed using the senescence b-galactosidase staining kit (Cell Signaling #9860). At least 10 randomly selected fields from the 20X magnification of the bright-field microscope (~500 cells) were imaged and counted.

For γH2AX foci formation assay, 2000 cells were seeded in Ibidi optical 96 well plates (SLS4515-5EA). Cells were fixed with 2% PFA at RT for 10 minutes. Fixed cells were permeabilized using 0.5% Triton-X in PBS and blocked with 10% BSA/PBS for 1h at RT before incubation with primary γH2AX antibody (1:500, cellSignaling#2577 overnight at 4°C. Cells were washed 3 times with DPBS and incubated with secondary Cy3-conjugated antibody (anti-rabbit). Images were acquired using an Incell Analyzer

2000. Image analysis and foci quantification was performed using Cell Profiler (v.4.0.7).

Western Blot

Western blots and antibodies are described elsewhere (14). Additional antibodies used in this study are anti-CIP2A (SantaCruz#sc-80662, 1:1000), anti-SET (SantaCruz# sc-133138,1:500), anti-phospho-Histone H2AX (Ser139) (cellSignaling#2577S, 1:1000), anti-PHAP1 (abcam#ab155148, 1:1000), anti-CHK1(Ser345) (CellSignaling,133D3, 2348, 1:1000), and anti-CHK2(Thr68) (CellSignaling,C13C1, 2197, 1:1000) and anti-PPP2CA (PP2A-Cα/β Antibody (1D6) HRP (LabForce,sc-80665 HRP,1:800)). Protein levels were normalized to total protein.

Flow Cytometry

Cells were fixed with cold methanol and incubated at RT with DAPI for 10 min in dark. Analysis of the cell cycle distribution was performed using a BD SORP LSR II flow cytometer connected to a BD FACSDiva software. Data was analyzed using FlowJo V10 (Tree Star,Inc.(Ashland, OR, USA)). As gating strategy, following elimination of dead cells and debris, G1 peak was used to adjust other peaks.

TCGA data analysis

CBioPortal and TCGABiolinks R packages were used for survival data analysis. Overall survival was defined as the time interval between date death/ last contact and the date of initial surgery.

Statistics

Statistical tests were performed using GraphPad Prism v.8.2.1 (GraphPad Software, San Diego, CA) and R studio v.4.0.3 (RStudio, Boston, MA). For comparing differences between two groups, non-parametric Mann-Whitney-U test was applied and p-values of <0.05 were considered as statistically significant. Unless otherwise

stated, at least three biological replicates and three technical replicates were included in each experiment.

Results

MicroRNA screen reproducibly identified miR-19b-3p enrichment by TMZ treatment

We transduced GBM cells with a lentiviral expression library containing 520 microRNA precursors (pri-miR) and cultured them at escalating doses of TMZ or DMSO control, with the aim to identify miRs implicated in TMZ resistance. Non-transduced cells did not survive this treatment regimen (suppl Fig.1A). Selection of resistant cells was monitored by PCR using primers encompassing pri-mRNA regions (suppl. Fig.1B). A discrete fragment pattern of PCR products, indicating complete selection, was first observed 46 days of TMZ treatment (suppl. Fig.1B). NGS analysis revealed that the relative coverage of pri-miR sequences correlated significantly in two independent screens of U87MG cells depending on the treatment condition (suppl.Fig.1C-D). Comparison of the normalized coverage of individual pri-miR sequences revealed significant enrichment for miR-19b/miR-20b in two independent U87MG screens and one LN229 screen (Fig. 1A). In contrast, other miRNAs were enriched exclusively in one cell line.

U87MG cells were transduced individually using expression constructs for miRs identified in U87MG screens and analyzed for TMZ response. In addition, miR-19b-2 and miR-20b, which form part of the same pre-miRNA, were overexpressed individually in U87MG cells. In agreement with the screen data, all miRs including miR-19b-2, miR-20b, miR-589, and miR-1302 conferred resistance to TMZ (Fig. 1B). Notably, miR-19b alone conferred improved survival in the presence of TMZ compared to miR-20b alone or miR-19b/20b combination. In addition, miR-19b expression was

associated with an unfavorable prognosis in our retrospective discovery cohort of GBM IDH wt patients (n=28) (Fig.1C). We therefore focused on miR-19b for subsequent experiments.

MiR-19b confers TMZ resistance in cell lines and GBM stem cells

Overexpression of miR-19b precursor (pmiR19b) conferred enhanced survival of U87MG cells treated with TMZ whereas overexpression of antisense miR-19b (αmiR19b) conferred reduced survival compared to precursor scrambled control (pscr) or antisense scrambled control (αscr), respectively (Fig.1D,left and suppl.Fig.2A). No significant difference in population growth was observed in DMSO control (Fig.1D, right). Thus, TMZ resistance mechanisms *in vitro* are regulated by endogenous miR-19b levels. Consistently, clonogenic growth in the presence of TMZ was significantly enhanced in pmiR19b (suppl. Fig. 3A), whereas αmiR19b showed reduced clonogenic growth of U87MG or LN229 cells (Fig. 1E).

Glioblastoma stem cells (GSCs) are responsible for growth and recurrence in the tumor tissue of patients. They show intrinsic resistance to radio-chemotherapy, which is due to their apoptosis resistance and increased DNA repair capacity (15). To assess if enhanced TMZ resistance is associated with intracellular miR-19b expression levels in GSCs, qRT-PCR analysis was performed. Indeed, miR-19b levels were higher in GSC3 and GSC4 compared to more differentiated LN229 and LN18 cells, whereas U87MG, which has retained stem cell features (16), showed intermediate miR-19b expression levels (suppl. Fig.3B).

GSC3 and GSC4 primary cultures showed moderate response to TMZ which is presumably due to MGMT promoter methylation (suppl. Table 1). Attenuation of miR-19b in GSC4 resulted in reduced viability in the presence of TMZ (suppl. Fig. 3C). In contrast, GSC3, which grows in large spheroids, gave rise to inconsistent results.

Cellular processes elicited by miR-19b in response to TMZ

Following extensive dsDNA breaks, TMZ induces cell cycle arrest in G2/M after the next round of replication due to activation of DNA damage response to initiate DNA repair mechanisms. We, therefore, aimed to assess to what extent miR-19b induces cell cycle arrest in response to TMZ treatment. The percentage of U87MG or LN229 control cells in G2/M increased three-fold compared to untreated cells following treatment with TMZ for two days, resulting in G2/M arrest in about 50% of the population (Fig.2, αscr). In contrast, attenuation of miR-19b resulted in less cells in G2/M, whereas overexpression of miR-19b resulted in more cells in G2/M (Fig. 2A).

To assess the percentage of cells able to escape cell cycle arrest, we performed 5-Bromo-2´-Deoxyuridine (BrdU) incorporation assay after the next round of replication of TMZ treatment. A higher proportion of pmiR19b cells, compared to pscr, was able to escape G2/M arrest in presence of TMZ, as indicated by a higher percentage of BrdU-positive cells in line with enhanced resistance (Fig. 2B). In the absence of TMZ, pmiR19b cells showed increased and α-miR19b cells showed reduced BrdU incorporation compared to the control (Fig. 2B) in agreement with its oncogenic role (14).

Extrinsic apoptosis triggered by the co-treatment with TNFα and actinomycin D (TNFα/ActD) was enhanced in αmiR19b cells compared to αscr, whereas the rate of spontaneous apoptosis was unaffected (Fig.2C, DMSO ctrl). Likewise, TMZ-induced apoptosis was slightly enhanced in αmiR19b cells (Fig.2C). Furthermore, αmiR19b cells showed a reduced kinetics of wound closure (Fig. 2D), which was only assessed in the absence of TMZ. In line with this finding, gene ontology and gene set enrichment analysis of the mRNA expression profile of both miR-19b overexpressing U87MG and LN229 cells showed enrichment of core extracellular matrix genes including ECM

glycoproteins, collagens, and proteoglycans (NABA MATRISOME). In addition, enhanced RAS pathway, membrane trafficking, extracellular matrix organization, and energy metabolism was noted in agreement with the oncogenic role of miR-19b in GBM (suppl.Fig.3D).

PPP2R5E subunit of PP2A is a target of miR19b

We previously showed that attenuation of miR-19b in NSCLC cells resulted in reduced phosphorylation at serine/threonine residues in line with our findings that miR-19b targets serine/threonine (S/T) phosphatase PP2A subunit PPP2R5E (14). Consistent with this finding, attenuation of miR-19b resulted in enhanced S/T activity (Fig.3A) and increased mRNA levels of PPP2R5E of GBM cells (Fig.3B). In addition, luciferase reporter assays, using a construct containing the miR-19b target site of PPP2R5E (TS), resulted in enhanced luciferase activity in αmiR19b compared to αsrc, while a construct in which the miR-19b target site of PPP2R5E was mutated (mTS) did not yield enhanced luciferase activity (Fig.3C). MiR-19b attenuation also resulted in reduced phospho-AKT (pAkt) consistent with PPP2R5E reactivation, but to our surprise, phospho-ERK (pErk) levels were enhanced (Fig. 3D). The pan-ERK and pan-AKT levels were unaffected suggesting that regulation was at the level of phosphorylation. We found that cellular inhibitor of PP2A (CIP2A), an endogenous inhibitor of PP2A, was upregulated in αmiR19b cells and downregulated in pmiR19b cells (Fig. 3D). The mechanism of CIP2A regulation by miR-19b is unknown. However, it is well established that CIP2A induction contributes to pErk activation (17).

We next assessed expression of miR-19b and PPP2R5E mRNA in the TCGA-GBM dataset (n=206). Interestingly, expression of PPP2R5E was inversely correlated with the expression of miR-19b in the mesenchymal molecular subtype, but not proneural, classical or neural subtypes of GBM (Fig. 3E). Consistent with this finding,

patients with low expression of PPP2R5E (z-score<-2) were more frequent in the mesenchymal (57%) and neural (52%) subtypes compared to classical (26%) and proneural (39%) subtypes, respectively (suppl.Fig.4).

The longitudinal cohort (n=43) consists of matched initial (therapy-naïve) and recurrent tumors with an interval of at least one year between pre-therapeutic and post-therapeutic resections, and 10 normal adjacent brain tissues (9). While miR-19b expression was significantly enhanced in initial tumors compared with normal tissue (Fig.3F), there was no significant inverse correlation of miR-19b and PPP2R5E expression in initial and recurrent tumors (Pearson R^2=0.003). Thus, although miR-19b/PPP2R5E regulatory axis plays an important role in intrinsic TMZ resistance, it seems not to be involved in GBM recurrence.

MiR-19b confers TMZ resistance by targeting PPP2R5E

We next investigated whether PPP2R5E knockdown (shPPP2R5E) phenocopies miR-19b overexpression in TMZ response pathways. Indeed, knocking down PPP2R5E conferred enhanced survival (Fig. 4A, lower and suppl Fig. 2B) and clonogenic growth (Fig. 4B, upper right) in the presence of TMZ, whereas shPPP2R5E cells showed only slightly increased 2-dimensional growth (Fig. 4A, upper) and clonogenic growth in the absence of TMZ (Fig. 4B, upper left). In contrast, knocking down PP2A catalytic subunit PPP2CA did not affect TMZ response (Fig.4A lower and 4B), although it reduced S/T phosphatase activity to an extent comparable to that of the PPP2R5E knockdown (suppl.Fig.2C), suggesting that PPP2R5E is the limiting component of PP2A complexes responsible for TMZ response. Consistent with the results of pmiR19b cells, the percentage of U87MG and LN229 cells in G2/M was higher in shPPP2R5E compared to sh(ctrl) following TMZ treatment (Fig. 4C). In addition, a higher proportion of shPPP2R5E relative to sh(ctrl) cells was able to escape

TMZ-induced cell cycle arrest, but shPPP2CA had no effect (Fig.4D). Consistent with our results in NSCLC (14) , pErk and pAkt levels were enhanced in shPPP2R5E cells (Fig. 4E). Likewise, gene set enrichment analysis revealed enrichment of EGFR signaling pathway (ERBB2, ERBB4, PI3K, AKT), and focal adhesion in shPPP2R5E cells, but these pathways were not enriched in shPPP2CA cells (suppl. Fig. 5A).

To assess if PPP2R5E acts via PP2A complexes, we aimed to activate PP2A using the small PP2A activator 2-amino-2-[2-(4-octylphenyl)] (FTY720), a synthetic sphingosine immuno-suppressor used for the treatment of multiple sclerosis (18). Indeed, FTY720 treatment resulted in reduced pAkt and pErk levels with fast kinetics (Fig.4F). In GSCs, TMZ and FTY720 acted synergistically to induce cell death at 100 (Fig. 4G, upper), 70 or 85 μM TMZ (suppl.Fig.5B).

We next investigated if miR-19b confers TMZ resistance by targeting PPP2R5E. In the presence of TMZ, αmiR19b conferred reduced viability whereas shPPP2R5E conferred enhanced viability, but co-transduction of LN229 cells with αmiR19b and shPPP2R5E (αmiR19b+shPPP2R5E) rescued the phenotype elicited by αmiR19b or shPPP2R5E alone (Fig.5A). These results were also confirmed by colony formation assay (Fig. 5B). In addition, decreased TMZ-induced G2/M arrest (Fig. 5C) and reduced migration (Fig. 5D) elicited by αmiR19b were rescued in αmiR19b/shPPP2R5E cells.

PP2A inhibiting proteins contribute to reduced PP2A activity and TMZ resistance

PP2A inhibiting proteins (PAIP) contribute to PP2A inactivation (19). In our cohort of recurrent GBM, CIP2A and PHAP1 were upregulated in recurrent tumors compared to matched initial tumors (Fig.6A). To assess their role in TMZ resistance, PAIP knockdown cell lines were generated using two different shRNAs constructs (suppl Table 2, and Suppl.Fig.2D-E). All shPAIPs showed enhanced Akt

phosphorylation and in addition, shSET, shPME1, and shPHAP1 showed enhanced Erk phosphorylation (Fig.6B). shPHAP1, shCIP2A#1 and shPME1 cells were more sensitive to TMZ compared to sh(ctrl) by clonogenic growth assay (Fig. 6C), induced more CHK2 (Fig. 6B), and a lower proportion of cells was able to escape cell cycle arrest (Fig. 6D).

Mechanism of enhanced TMZ-induced DNA damage response elicited by αmiR19b

γH2AX foci formation is a dynamic process, triggered by the formation of DSBs, and its removal by the repair machinery of the damaged DNA (20). γH2AX foci formation was induced following TMZ treatment after the second round of replication (αscr, Fig.7A). TMZ-induced γH2AX foci formation and expression was strongly enhanced in αmiR19b LN229 (Fig.7A and suppl.Fig.6A) and U87MG cells (suppl. Fig. 6B), but this phenotype was restored in αmiR19b/shPPP2R5E cells (Fig.7A). Consistent results, although at lower foci counts, were also observed in DMSO treated LN229 (Fig.7A), U87MG (suppl. Fig. 6B, left) and GSC4 (suppl. Fig. 6C). To assess γH2AX foci clearance, cells were pulsed-treated with TMZ for 5h and γH2AX foci formation analysis was performed during the recovery period. Comparable kinetics of γH2AX foci formation and clearance was obtained in αscr, αmiR19b and αmiR19b+shPPP2R5E (suppl. Fig. 6D), suggesting that enhanced γH2AX foci elicited by αmiR19b was not due to delayed foci clearance. αmiR19b cells presented with enlarged and granular morphology reminiscent of senescent cells (Fig.7A, brightfield channel). Indeed, αmiR19b cells expressed elevated β-galatosidase (SA-β-gal) levels compared to αscr in the absence of TMZ and this phenotype was rescued in αmiR+PPP2R5E cells. TMZ treatment strongly induced SA-β-gal expression, but again

higher levels were obtained in αmiR19b compared to αscr and αmiR/PPP2R5E cells (Fig.7B). In addition, TMZ-induced phosphorylation of CHK1 and CHK2 were enhanced in αmiR19b cells but reduced in shPPP2R5E cells. Conversely, FTY720 treatment enhanced TMZ-induced phosphorylation of CHK1 and CHK2, which was again reversed in shPPP2R5E cells (Fig.7C), confirming that PP2A complexes containing PPP2R5E sensitize GSCs for TMZ response.

PPP2R5E knockdown induces TMZ resistance in vivo

We next assessed TMZ response of shPPP2R5E *in vivo*. To this end, we established a patient-derived xerograph (PDX) mouse model using GSC4 cells orthotopically injected into the right hemisphere of nude immune compromised mice. GSC4 was transduced with beetle luciferase reporter construct allowing for monitoring tumor growth using an in vivo imaging system (IVIS). Mice received five cycles of TMZ per week, which was re-challenged after 4 and 8 weeks (Fig. 8A), a protocol normally used for the treatment of human patients. Unexpectedly, tumor engraftment prior to initiating therapy was significantly compromised in shPPP2R5E as indicated by a smaller tumor volume 11 days post xenografting compared to sh(ctrl) (Fig. 8B). In addition, 92% (22/24) of GSC4-sh(ctrl) mice, but only 76% (16/21) of GSC4-shPPP2R5E mice developed tumors. However, once tumors had been established, shPPP2R5E developed larger tumors despite standard of care (Fig. 8C). shPPP2R5E tumors were more aggressive than sh(ctrl) as indicated by Ki67 staining (Fig. 8D). A tendency towards enhanced β-catenin and SMAD2/3 activity, known mediators of stem cell maintenance and proliferation following TMZ treatment (21), was detected in shPPP2R5E tumors, whereas expression of SOX9, a protein involved in differentiation, migration and invasion of GBM (22), was reduced (Fig. 8D).

Interestingly, we found that GSC4 tumors were able to form distant metastasis to the left hemisphere and distant spinal cord (Fig.8E). GSC4 does not invade into the brain parenchyma, a finding also confirmed in distant metastases to the spinal cord (Fig. 8F). While there were no significant differences in frequency of metastases in shPPP2R5E and sh(ctrl) tumors, the tumor volume at metastatic sites was significantly larger in PPP2R5E tumors compared to sh(ctrl) (Fig. 8G).

Discussion:

We performed a microRNA screening with the aim to identify TMZ resistance mechanisms in GBM. A lentiviral construct expressing the miR19b/20b hairpin was the only construct consistently selected by TMZ in two GBM cell lines. miR-19b and miR-20b form part of oncomiR-1, a miR cluster, which acts as oncogenic driver of B-cell lymphomas and lung cancer (23) . MiR-19b is a key oncogenic component of oncomiR-1 implicated in proliferation, apoptosis, invasion (reviewed by (24)) and drug resistance in breast cancer (25) and NSCLC (14). It is also significantly up-regulated in glioma tissues and positively correlates with the glioma grade (26). MiR-19b expression is associated with an unfavorable prognosis of GBM patients (27,28), a finding also confirmed in our study (Fig. 1C).

To the best of our knowledge, this is the first study showing that miR-19b is implicated in TMZ resistance of GBM. TMZ-induced γH2AX foci formation, CHK1/CHK2 phosphorylation and senescence were significantly enhanced, while TMZ-induced G2/M arrest was reduced in miR-19b attenuated GBM cell lines and GSCs indicating elevated DNA damage. In line with these findings, treating cells with FTY720, which restores PP2A activity by interacting with CIP2A and SET (29) , or knocking down CIP2A, PME1 or PHAP1 enhanced TMZ sensitivity mediated by PPP2R5E reactivation. This gene frequently downregulated, but rarely mutated in

GBM (19). Orthotopic mouse experiments revealed that GSC4 shPPP2R5E tumors were more aggressive and less responsive to TMZ compared to sh(ctrl). 2% of intracranial, and up to 25% of supratentorial GBM can disseminate to other locations including spinal cord (30). Attenuation of PPP2R5E did not affect dissemination, but it also affected tumor response at the metastatic site. Unexpectedly, tumor engraftment was compromised in shPPP2R5E tumors, suggesting that establishment of the GBM niche or adaptation to the murine microenvironment might be disturbed.

It is well established that PP2A complexes dephosphorylate CHK1, CHK2 and ATM, and thereby interfere with DNA damage response and double-strand DNA break repair (31,32), which was confirmed using inhibitors of CHK1 and CHK2 (33). We show that the kinetics of TMZ-induced γH2AX foci clearance was not altered in αmiR19b, sh(ctrl) and αmiR19b/shPPP2R5E cells suggesting that DNA damage response was not the main cause of enhanced TMZ response. Instead, attenuation of miR-19b caused persistent DNA damage in the absence of TMZ. Hence, more DNA damage is caused by the combination of TMZ and αmiR19b (or other means of PPP2R5E reactivation) than with TMZ or αmiR19b alone (Fig. 7D). Conversely, overexpression of miR-19b (or PPP2R5E repression) may inhibit cellular senescence and enhanced TMZ resistance. The mechanism of DNA damage elicited by PPP2R5E reactivation is unknown. PP2A induction is associated with enhanced senescence in melanoma (34), KRAS-driven lung cancer (35) and GBM (36), but the underlying mechanism is unknown. Phosphoproteomics and transcriptomics analysis revealed a role of PP2A holoenzyme in metabolic enzyme induction and NRF2-mediated oxidative stress response pathways (37), which may lead to elevated ROS production, and DNA damage. Mitochondrial dysfunction, which results in elevated ROS production, is a hallmark of cellular senescence (38). Thus, an alternative explanation may be that DNA damage is caused ensuing PPP2R5E-induced senescence.

Our results suggest that reactivation of PPP2R5E by means of αmiR19b could be used therapeutically to sensitize tumors to TMZ/RT response, whereas FTY720 or other PAIP interfering drugs are associated with more severe side effects, since multiple PP2A complexes are affected. PPP2R5E reactivation in the recurrent tumor seems to be mediated by upregulation of CIP2A and PHAP1. Hence, although miR-19b is not directly implicated in recurrence, αmiR19b therapy may still be effective. The miR-19b/PPP2R5E axis induces migration, which could also be exploited therapeutically to interfere with the infiltrative growth of GBM, but this could not be addressed in vivo due to the non-infiltrative growth pattern of GSC4. Multiple miR-based therapies have entered clinical phase I and II trials for the treatment of different types of cancer and other diseases (reviewed by (39)). Although none of these clinical trials are related to the brain, miR-based therapies indicate great potential also for CNS tumors (40).

In summary, our results demonstrate that PPP2R5E reactivation by inhibiting miR-19b or PP2A inhibitory proteins can re-sensitize GBM cells to TMZ. More experiments are needed to elucidate the synergism of DNA damage elicited by TMZ and PPP2R5E reactivation.

Acknowledgements

We thank Eugenio Zoni and Marianna Kruithof-de Julio, DBMR, University of Bern, for constructs and help with the IVIS instrument, Mario Tschan, Institute of Pathology, University of Bern, and Ren-Wang Peng, DBMR, University of Bern, for providing antibodies.

References

1. Louis DN, Perry A, Wesseling P, Brat DJ, Cree IA, Figarella-Branger D, et al. The 2021 WHO classification of tumors of the central nervous system: A summary. Neuro Oncol. Oxford University Press; 2021;23:1231–51.
2. Knizhnik A V., Roos WP, Nikolova T, Quiros S, Tomaszowski KH, Christmann M, et al. Survival and Death Strategies in Glioma Cells: Autophagy, Senescence and Apoptosis Triggered by a Single Type of Temozolomide-Induced DNA Damage. 2013;8.
3. Hegi ME, Diserens A-C, Gorlia T, Hamou M-F, De Tribolet N, Weller M, et al. MGMT Gene Silencing and Benefit from Temozolomide in Glioblastoma. N Engl J Med. 2005;352:997–1003.
4. Del Alcazar CRG, Todorova PK, Habib AA, Mukherjee B, Burma S. Augmented HR repair mediates acquired temozolomide resistance in glioblastoma. Mol Cancer Res. 2016;14:928–40.
5. Kitange GJ, Mladek AC, Carlson BL, Schroeder MA, Pokorny JL, Cen L, et al. Inhibition of histone deacetylation potentiates the evolution of acquired temozolomide resistance linked to MGMT upregulation in glioblastoma xenografts. Clin Cancer Res. 2012;18:4070–9.
6. Yamashiro K, Nakao K, Ohba Sh HY. Human Glioma Cells Acquire Temozolomide Resistance After Repeated Drug Exposure Via DNA Mismatch Repair Dysfunction. Anticancer Res. 2020;40:1315–23.
7. Zhang X, Li T, Yang M, Du Q, Wang R, Fu B, et al. Acquired temozolomide resistance in MGMTlow gliomas is associated with regulation of homologous recombination repair by ROCK2. Cell Death Dis. Springer US; 2022;13.
8. Barthel FP, Johnson KC, Varn FS, Moskalik AD, Tanner G, Kocakavuk E, et al. Longitudinal molecular trajectories of diffuse glioma in adults. Nature. Springer US; 2019;576:112–20.

9. Kashani E, Schnidrig D, Gheinani AH, Ninck MS, Zens P, Maragkou T, et al. Integrated longitudinal analysis of adult grade 4 diffuse gliomas with long-term relapse interval revealed upregulation of TGF-β signaling in recurrent tumors. Neuro Oncol. 2022;

10. Peraza-Vega RI, Valverde M, Rojas E. Interactions between miRNAs and Double-Strand Breaks DNA Repair Genes, Pursuing a Fine-Tuning of Repair. Int J Mol Sci. 2022;23.

11. Haemmig S, Baumgartner U, Glück A, Zbinden S, Tschan MP, Kappeler A, et al. MiR-125b controls apoptosis and temozolomide resistance by targeting TNFAIP3 and NKIRAS2 in glioblastomas. Cell Death Dis. Nature Publishing Group; 2014;5.

12. Luedi MM, Singh SK, Mosley JC, Hassan ISA, Hatami M, Gumin J, et al. Dexamethasone-mediated oncogenicity in vitro and in an animal model of glioblastoma. J Neurosurg. 2018;129:1446–55.

13. Hall MP, Woodroofe CC, Wood MG, Que I, Van'T Root M, Ridwan Y, et al. Click beetle luciferase mutant and near infrared naphthyl-luciferins for improved bioluminescence imaging. Nat Commun. Nature Publishing Group; 2018;9.

14. Baumgartner U, Berger F, Hashemi Gheinani A, Burgener SS, Monastyrskaya K, Vassella E. miR-19b enhances proliferation and apoptosis resistance via the EGFR signaling pathway by targeting PP2A and BIM in non-small cell lung cancer. Mol Cancer. Molecular Cancer; 2018;17:1–15.

15. Annovazzi L, Caldera V, Mellai M, Riganti C, Battaglia L, Chirio D, et al. The DNA damage/repair cascade in glioblastoma cell lines after chemotherapeutic agent treatment. Int J Oncol. Spandidos Publications; 2015;46:2299–308.

16. Oh SJ, Yang JI, Kim O, Ahn EJ, Kang WD, Lee JH, et al. Human U87 glioblastoma cells with stemness features display enhanced sensitivity to natural

killer cell cytotoxicity through altered expression of NKG2D ligand. Cancer Cell Int. BioMed Central; 2017;17:1–9.

17. Chen KF, Yen CC, Lin JK, Chen WS, Yang SH, Jiang JK, et al. Cancerous inhibitor of protein phosphatase 2A (CIP2A) is an independent prognostic marker in wild-type KRAS metastatic colorectal cancer after colorectal liver metastasectomy. BMC Cancer. 2015;15:1–9.
18. Kappos L, Radue E-W, O'connor P, Polman C, Hohlfeld R, Calabresi P, et al. A Placebo-Controlled Trial of Oral Fingolimod in Relapsing Multiple Sclerosis. n engl j med. 2010;362:387–401.
19. Kashani E, Vassella E. Pleiotropy of PP2A Phosphatases in Cancer with a Focus on Glioblastoma IDH Wildtype. Cancers (Basel). 2022;14:5227.
20. Mariotti LG, Pirovano G, Savage KI, Ghita M, Ottolenghi A, Prise KM, et al. Use of the γ-H2AX assay to investigate DNA repair dynamics following multiple radiation exposures. PLoS One. 2013;8:1–12.
21. Ulasov I V., Nandi S, Dey M, Sonabend AM, Lesniak MS. Inhibition of sonic hedgehog and notch pathways enhances sensitivity of cd133+ glioma stem cells to temozolomide therapy. Mol Med. 2011;17:103–12.
22. Chao M, Liu N, Sun Z, Jiang Y, Jiang T, Xv M, et al. TGF-β Signaling Promotes Glioma Progression Through Stabilizing Sox9. Front Immunol. 2021;11:1–10.
23. Cho WCS. OncomiRs: The discovery and progress of microRNAs in cancers. Mol Cancer. 2007;6:1–7.
24. Wang W, Zhang A, Hao Y, Wang G, Jia Z. The emerging role of miR-19 in glioma. 2018;
25. Liang Z, Li Y, Huang K, Wagar N, Shim H. Regulation of miR-19 to breast cancer chemoresistance through targeting PTEN. Pharm Res. 2011;28:3091–100.
26. Jia Z, Wang K, Zhang A, Wang G, Kang C, Han L, et al. MiR-19a and miR-19b

overexpression in gliomas. Pathol Oncol Res. 2013;19:847–53.

27. Schnabel E, Knoll M, Schwager C, Warta R, Mock A, Campos B, et al. Prognostic value of microRNA-221/2 and 17-92 families in primary glioblastoma patients treated with postoperative radiotherapy. Int J Mol Sci. 2021;22:1–18.
28. Zhi F, Shao N, Wang R, Deng D, Xue L, Wang Q, et al. Identification of 9 serum microRNAs as potential noninvasive biomarkers of human astrocytoma. Neuro Oncol. 2015;17:383–91.
29. Cristóbal I, Madoz-Gúrpide J, Manso R, González-Alonso P, Rojo F, García-Foncillas J. Potential anti-tumor effects of FTY720 associated with PP2A activation: a brief review. Curr Med Res Opin. Taylor & Francis; 2016;32:1137–41.
30. Shah A, Redhu R, Nadkarni T, Goel A. Supratentorial glioblastoma multiforme with spinal metastases. J Craniovertebr Junction Spine. 2010;1:126–9.
31. Freeman, a; Dapic, V; Monteiro A. Chk2/Pp2a&DNAdamage. Cell cycle. 2011;9:736–47.
32. Leung-Pineda V, Ryan CE, Piwnica-Worms H. Phosphorylation of Chk1 by ATR Is Antagonized by a Chk1-Regulated Protein Phosphatase 2A Circuit. Mol Cell Biol. 2006;26:7529–38.
33. Ozgiray E, Sogutlu F, Biray Avci C. Chk1/2 inhibitor AZD7762 enhances the susceptibility of IDH-mutant brain cancer cells to temozolomide. Med Oncol. Springer US; 2022;39:1–14.
34. Mannava S, Omilian AR, Wawrzyniak JA, Fink EE, Zhuang D, Miecznikowski JC, et al. PP2A-B56α controls oncogene-induced senescence in normal and tumor human melanocytic cells. Oncogene. Nature Publishing Group; 2012;31:1484–92.
35. Kauko O, O'Connor CM, Kulesskiy E, Sangodkar J, Aakula A, Izadmehr S, et al.

PP2A inhibition is a druggable MEK inhibitor resistance mechanism in KRAS-mutant lung cancer cells. Sci Transl Med. 2018;10.

36. Cucinotta L, Filippone A, Casili G, Lanza M, Bova V, Capra AP, et al. The Pivotal Role of Protein Phosphatase 2A (PP2A) in Brain Tumors. Int J Mol Sci. 2022;23.
37. Chen L, Guo P, Li W, Jiang X, Zhao Q, Li D, et al. Protein phosphatase 2A regulates cytotoxicity and drug resistance by dephosphorylating AHR and MDR1. J Biol Chem. 2022;298:101918.
38. Shmulevich R, Krizhanovsky V. Cell Senescence, DNA Damage, and Metabolism. Antioxidants Redox Signal. 2021;34:324–34.
39. Chakraborty C, Sharma AR, Sharma G, Lee SS. Therapeutic advances of miRNAs: A preclinical and clinical update. J Adv Res. Cairo University; 2021;28:127–38.
40. Sun P, Liu DZ, Jickling GC, Sharp FR, Yin KJ. MicroRNA-based therapeutics in central nervous system injuries. J Cereb Blood Flow Metab. 2018;38:1125–48.

Figure legends

Fig1. Systematic miRNA screen identifies miR-19b implicated in TMZ resistance. **(A)** U87MG and LN229 cells transduced with pooled pri-miRNA library and reproducibly enriched >5-fold following TMZ treatment relative to the DMSO control ($p<0.028$). **(B)** Cell viability by alamarBlue of U87MG cells transduced with miRNAs identified in (A) following treatment with TMZ for 72 h relative to pscr (n=3). **(C)** Overall survival of GBM IDH wt patients from the discovery cohort expressing high or low levels of miR-19b by RT-qPCR (n=3). **(D)** Cell viability by alamarBlue of U87MG cells transduced with miR constructs in presence of TMZ (left) or DMSO control (right). **(E)** Colony formation (left) and representative images of crystal violet-stained colonies (right) of U87MG cells in the presence of continuous treatment with TMZ (n=3).

Fig2. Cellular processes elicited by miR-19b. **(A)** Cell cycle distribution following TMZ treatment (mean±SD, n=3). **(B)** BrdU incorporation assay of U87MG cells 4 days post treatment with TMZ (n=4). **(C)** Apoptosis induced with TNFα/ActD or 200uM TMZ by caspase 3/7 activity assay. **(D)** Left: Kinetics of wound closure of LN229 cells after 36h post scratch (n=3). Data is normalized to initial would size. Right: representative image of the same region immediately after scratch and 12h post scratch.

Fig3. miR-19b targets PP2A regulatory subunit PPP2R5E. **(A)** S/T phosphatase activity assay of αmiR19b U87MG cells (n=5). **(B)** PPP2R5E expression relative to GAPDH in αmiR-19b cells by RTqPCR (n=4). **(C)** Luciferase activity assay of a reporter construct containing a 3' untranslated region encompassing the miR-19b-3p target site of PPP2R5E (TS) or mutations in the miR-19b target site (mTS) (n=4). **(D)** Western blot analysis of αmiR19b and pmiR19b cells relative to control. Signal intensity of antibodies was normalized to total protein. **(E)** Inverse Pearson correlation of miR19b

and PPP2R5E mRNA in the mesenchymal subtype (n=56) (upper), proneural (n=56), classical (n=54), neural (n=29) subtypes or all subtypes together (n=206), (lower) from GBM-TCGA dataset. **(F)** PPP2R5E and miR19b mRNA expression in recurrent GBM relative to matched initial GBM.

Fig4. PPP2R5E is implicated in TMZ response. **(A)** Cell viability by alamarBlue of shPPP2R5E U87MG cells in the presence of DMSO for 4 days (upper) or TMZ for 8 days (lower) (n=3). **(B)** Colony formation assay of shPPP2R5E U87MG cells in presence of continuous treatment with 30μM TMZ or DMSO control (n=3). **(C)** Cell cycle position following treatment with TMZ for 48h (mean±SD, n=3). **(D)** BrdU incorporation assay. **(E)** Western blot analysis. pAkt/Akt and pErk/Erk indicate the signal ratio of phospho-specific antibody and pan-antibody. **(F)** Time-dependent phosphorylation of AKT and ERK following treatment with 5μM FTY720 in U87MG and corresponding Western blots. **(G)** AlamarBlue viability assay (upper) and Western blot analysis performed 48 days post treatment with 5uM FTY720 or TMZ.

Fig5. Phenotypes elicited by shPPP2R5E and αmiR19b cells are rescued in αmiR19b+shPPP2R5E cells. **(A)** Cell viability by alamarBlue (n=4), **(B)** colony formation assay (n=3) and **(C)** cell cycle position (n=1) following TMZ treatment. **(D)** Kinetics of wound closure and representative regions immediately after scratching and 12h post-scratching. Results for αscr and αmiR19b are the same as in Fig. 2D.

Fig6. PP2A inhibiting proteins (PAIPs) are upregulated in recurrent GBM and contribute to TMZ resistance. **(A)** Expression of PAIPs in normal brain tissues and patient matched initial and recurrent GBM. **(B)** Western blot analysis, **(C)** Colony

formation assay in presence of 20uM TMZ (n=3) and **(D)** BrdU incorporation assay (n=4) of U87MG cells transduced with shPAIPs constructs.

Fig7. DNA damage and senescence induced by miR-19b attenuation is enhanced by TMZ treatment. **(A)** γH2AX foci counts of DMSO or TMZ-treated LN229 cells (left) and merged representative images (60X magnification) in bright field, DAPI nuclei) and Cy3 (γH2AX foci). Foci were quantified by CellProfiler. The mean (n>10000) from two biological replicates is indicated by a horizontal blue line. **(B)** Percent β-galatosidase-positive DMSO or TMZ treated LN229 cells (n=4) (upper) and representative images in bright field (lower). **(C)** Western blot of pCHK1 and pCHK2 of GSC3 following treatment with TMZ for 2 days. **(D)** Model of synergism of DNA damage elicited by TMZ treatment and PPP2R5E reactivation.

Fig8. GSC4 orthotopic mouse model. **(A)** TMZ treatment scheme and monitoring of tumor size. **(B)** Tumor volume by the IVIS imaging 11 days post-xenografting prior to initiating TMZ treatment. **(C)** Tumor volume 52 days post-xenografting following two cycles of TMZ treatment. **(D)** Immunohistochemical analysis of tumors from mice euthanized at onset of neurological symptoms. **(E)** Example of IVIS images of sh(ctrl) and shPPP2R5E mice 74 days post-xenografting with spinal cord metastasis. **(F)** H&E-stained slide from spinal cord metastasis of shPPP2R5E tumor 74 days post-xenografing. (G) Tumor volume from metastatic site relative to primary tumor 32 days post-xenografing.

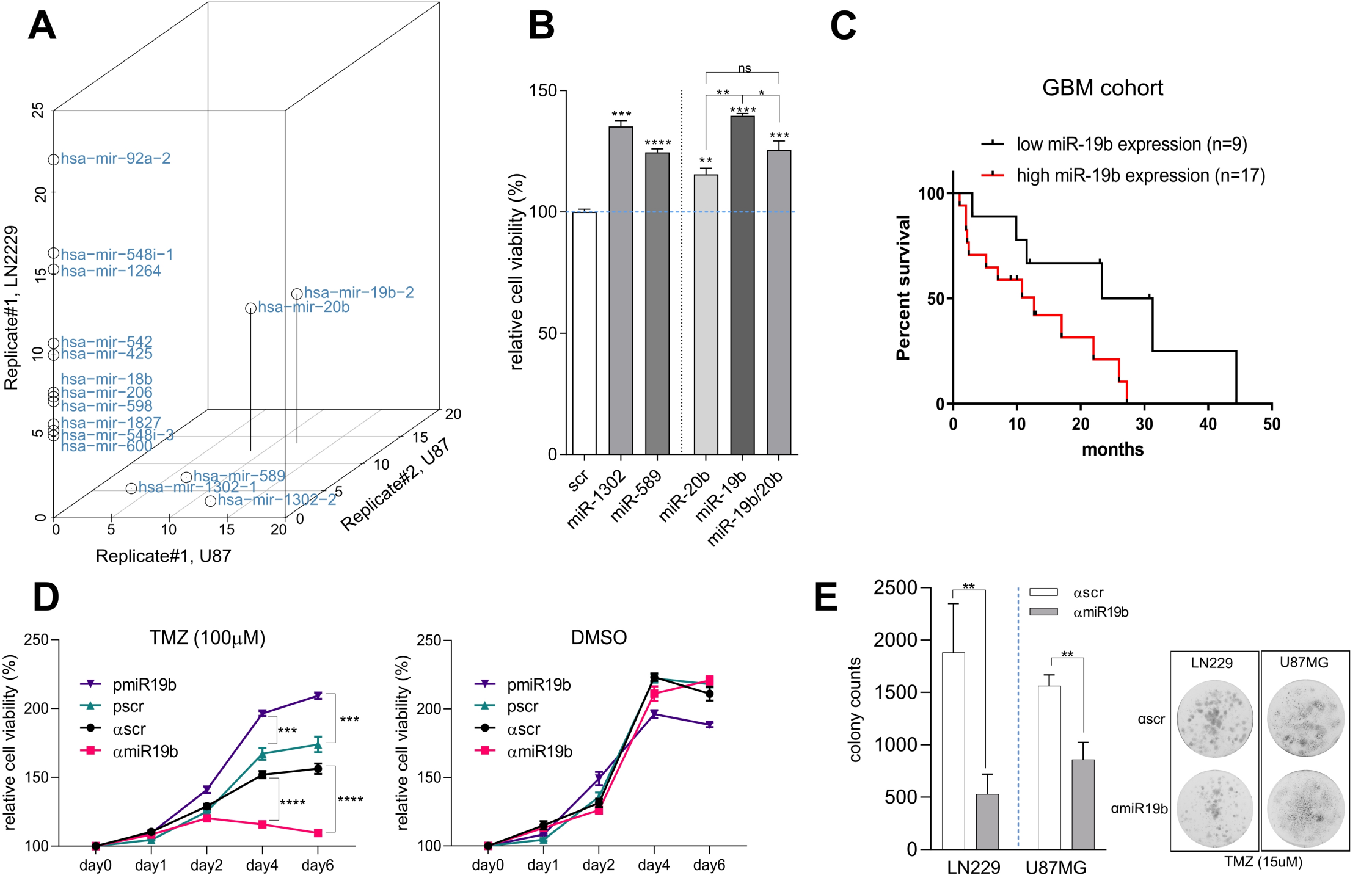
A
hsa−mir−92a−2
hsa−mir−548i−1
hsa−mir−1264
hsa−mir−19b−2
hsa−mir−20b
hsa−mir−542
hsa−mir−425
hsa−mir−18b
hsa−mir−206
hsa−mir−598
hsa−mir−1827
hsa−mir−548i−3
hsa−mir−600
hsa−mir−589
hsa−mir−1302−1
hsa−mir−1302−2
Replicate#1, LN2229
Replicate#1, U87
Replicate#2, U87
B
relative cell viability (%)
scr
miR-1302
miR-589
miR-20b
miR-19b
miR-19b/20b
ns
C
GBM cohort
low miR-19b expression (n=9)
high miR-19b expression (n=17)
Percent survival
months
D
TMZ (100μM)
DMSO
pmiR19b
pscr
αscr
αmiR19b
relative cell viability (%)
day0
day1
day2
day4
day6
E
αscr
αmiR19b
colony counts
LN229
U87MG
TMZ (15uM)

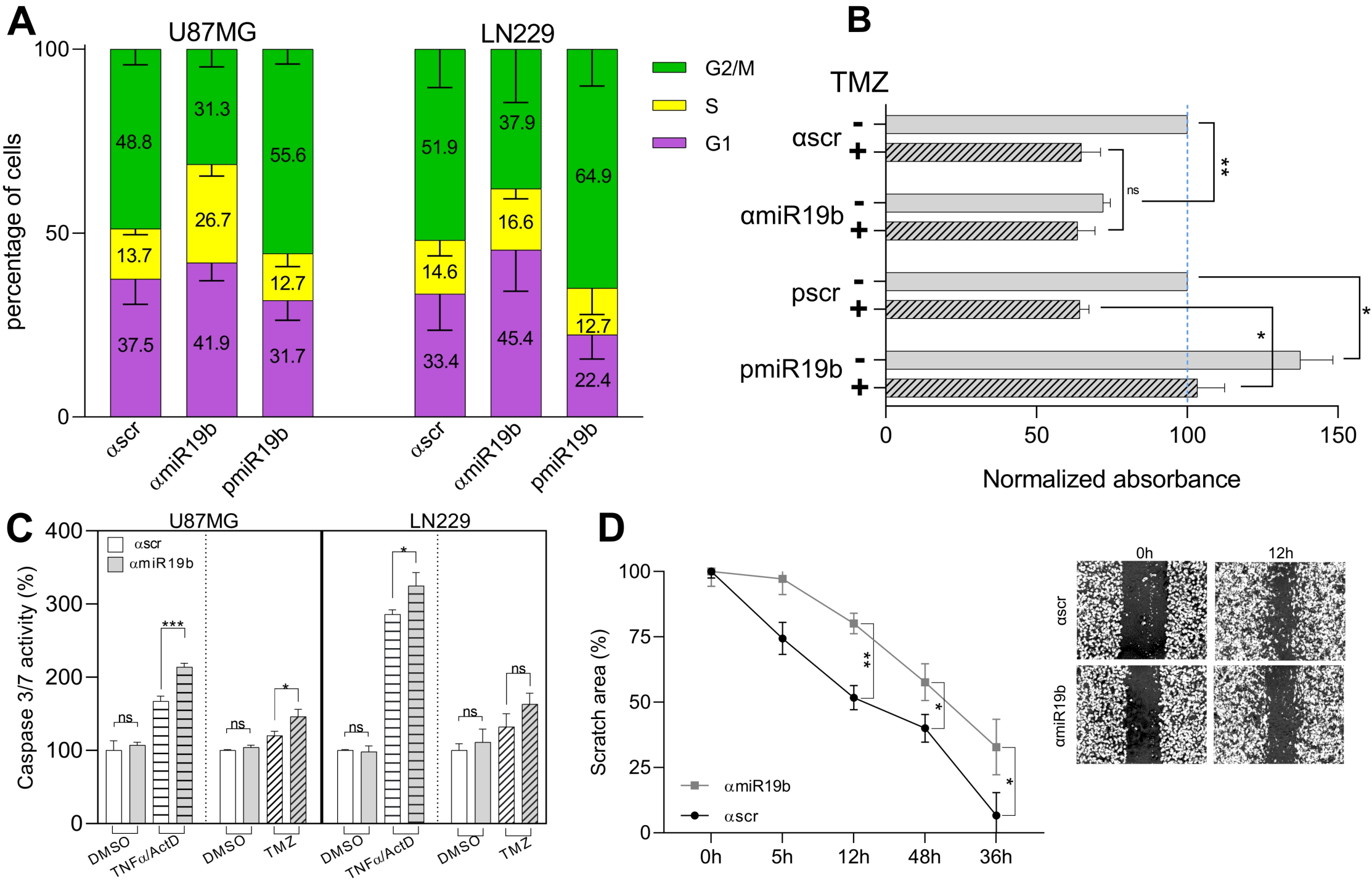
A
U87MG
LN229
percentage of cells
100
50
0
G2/M
S
G1
48.8
13.7
37.5
31.3
26.7
41.9
55.6
12.7
31.7
51.9
14.6
33.4
37.9
16.6
45.4
64.9
12.7
22.4
αscr
αmiR19b
pmiR19b
αscr
αmiR19b
pmiR19b
B
TMZ
αscr
αmiR19b
pscr
pmiR19b
-
+
ns
**
*
*
0
50
100
150
Normalized absorbance
C
U87MG
LN229
αscr
αmiR19b
Caspase 3/7 activity (%)
400
300
200
100
0
***
*
*
ns
ns
ns
ns
ns
ns
DMSO
TNFα/ActD
DMSO
TMZ
DMSO
TNFα/ActD
DMSO
TMZ
D
Scratch area (%)
100
75
50
25
0
αmiR19b
αscr
**
*
*
0h
5h
12h
48h
36h
0h
12h
αscr
αmiR19b

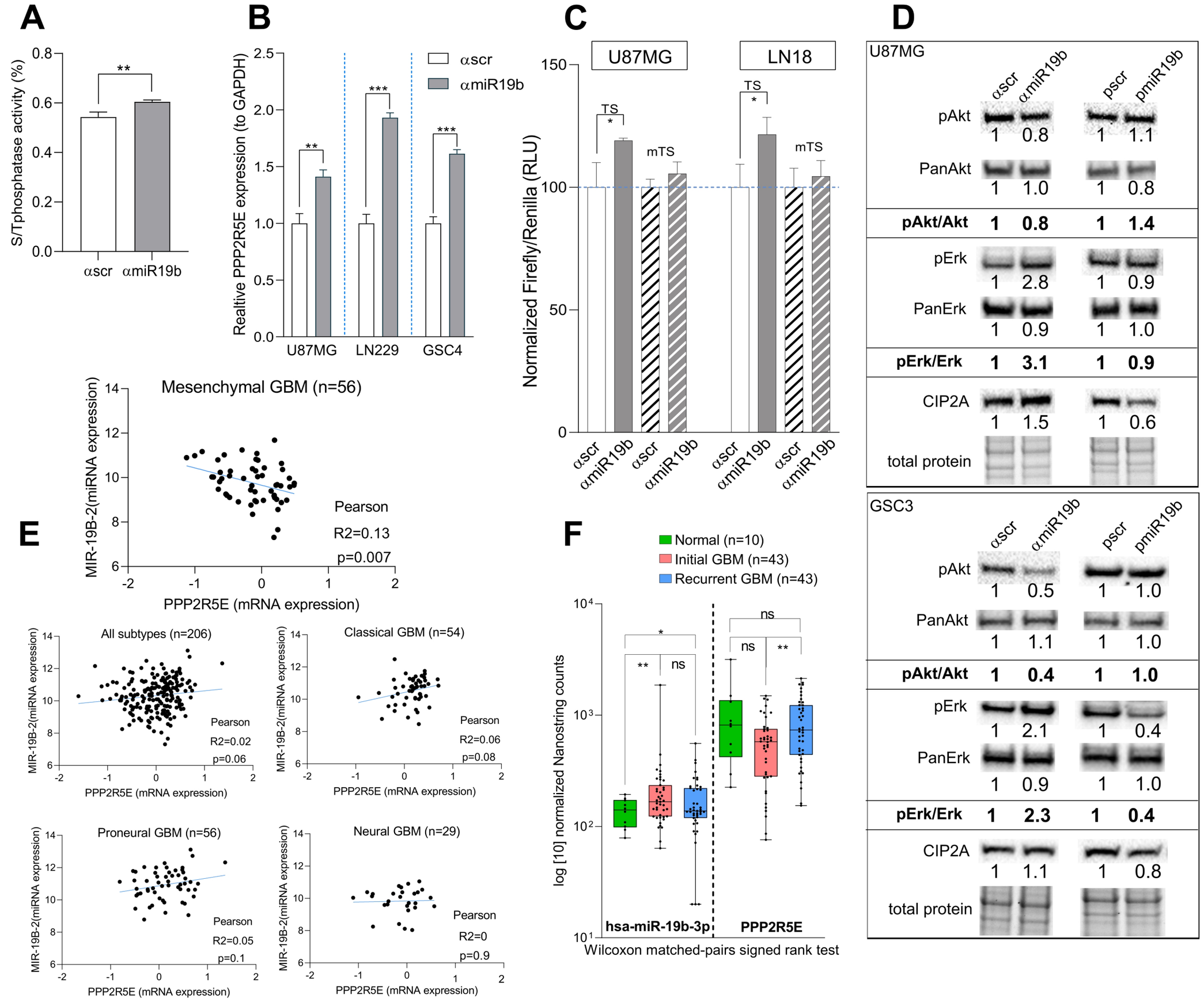
A
S/Tphosphatase activity (%)
αscr
αmiR19b
B
Realtive PPP2R5E expression (to GAPDH)
αscr
αmiR19b
U87MG
LN229
GSC4
C
U87MG
LN18
Normalized Firefly/Renilla (RLU)
TS
mTS
αscr
αmiR19b
D
U87MG
αscr
αmiR19b
pscr
pmiR19b
pAkt
PanAkt
pAkt/Akt
pErk
PanErk
pErk/Erk
CIP2A
total protein
GSC3
E
Mesenchymal GBM (n=56)
MIR-19B-2(miRNA expression)
PPP2R5E (mRNA expression)
Pearson
R2=0.13
p=0.007
All subtypes (n=206)
R2=0.02
p=0.06
Classical GBM (n=54)
R2=0.06
p=0.08
Proneural GBM (n=56)
R2=0.05
p=0.1
Neural GBM (n=29)
R2=0
p=0.9
F
Normal (n=10)
Initial GBM (n=43)
Recurrent GBM (n=43)
log [10] normalized Nanostring counts
hsa-miR-19b-3p
PPP2R5E
Wilcoxon matched-pairs signed rank test
ns

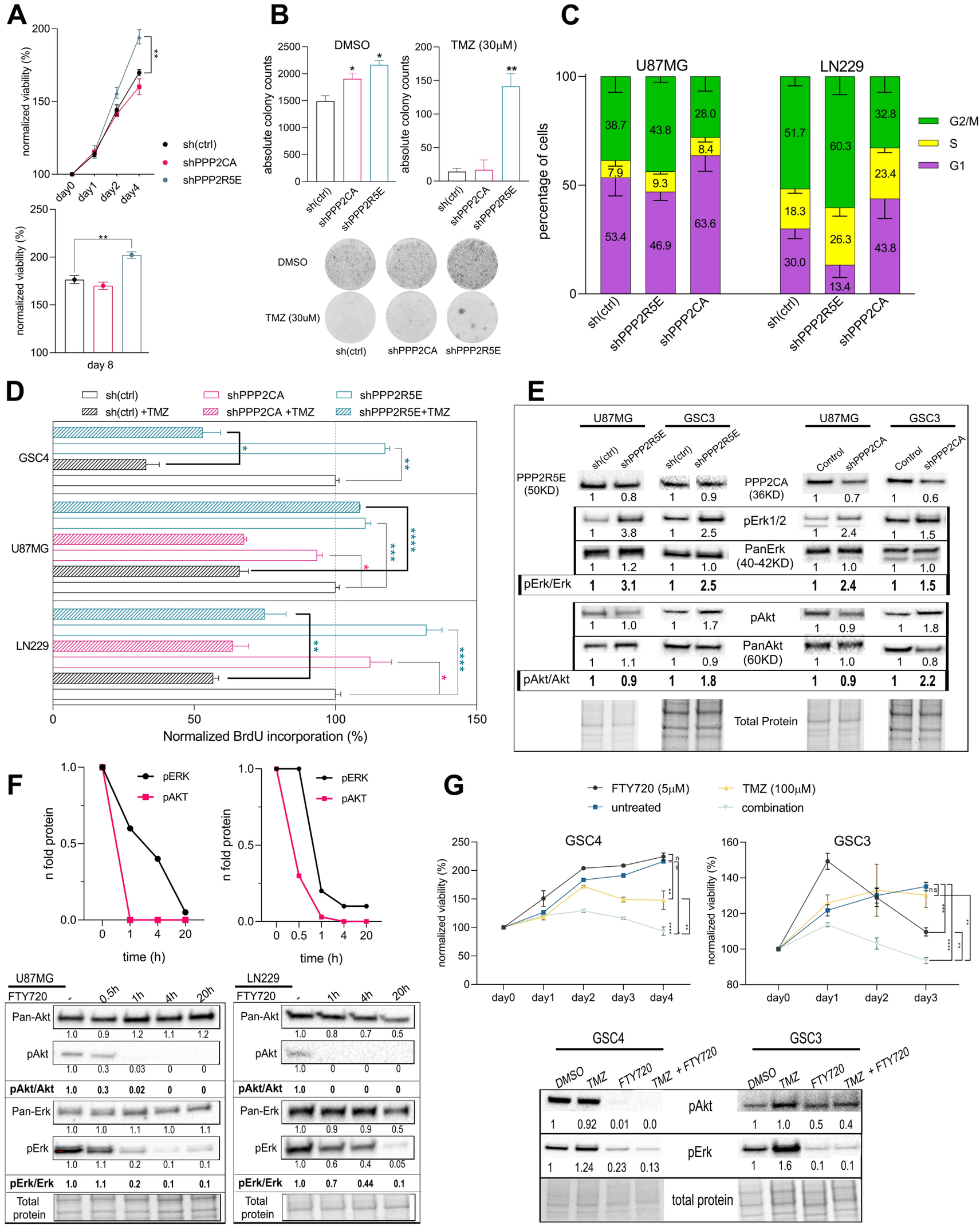
A
normalized viability (%)
day0
day1
day2
day4
sh(ctrl)
shPPP2CA
shPPP2R5E
day 8
B
DMSO
TMZ (30μM)
absolute colony counts
sh(ctrl)
shPPP2CA
shPPP2R5E
TMZ (30uM)
C
U87MG
LN229
percentage of cells
G2/M
S
G1
D
sh(ctrl) +TMZ
shPPP2CA +TMZ
shPPP2R5E+TMZ
GSC4
U87MG
LN229
Normalized BrdU incorporation (%)
E
U87MG
GSC3
Control
PPP2R5E (50KD)
PPP2CA (36KD)
pErk1/2
PanErk (40-42KD)
pErk/Erk
pAkt
PanAkt (60KD)
pAkt/Akt
Total Protein
F
pERK
pAKT
n fold protein
time (h)
FTY720
Pan-Akt
pAkt
pAkt/Akt
Pan-Erk
pErk
pErk/Erk
Total protein
G
FTY720 (5μM)
TMZ (100μM)
untreated
combination
GSC4
GSC3
normalized viability (%)
DMSO
TMZ
FTY720
TMZ + FTY720
pAkt
pErk
total protein

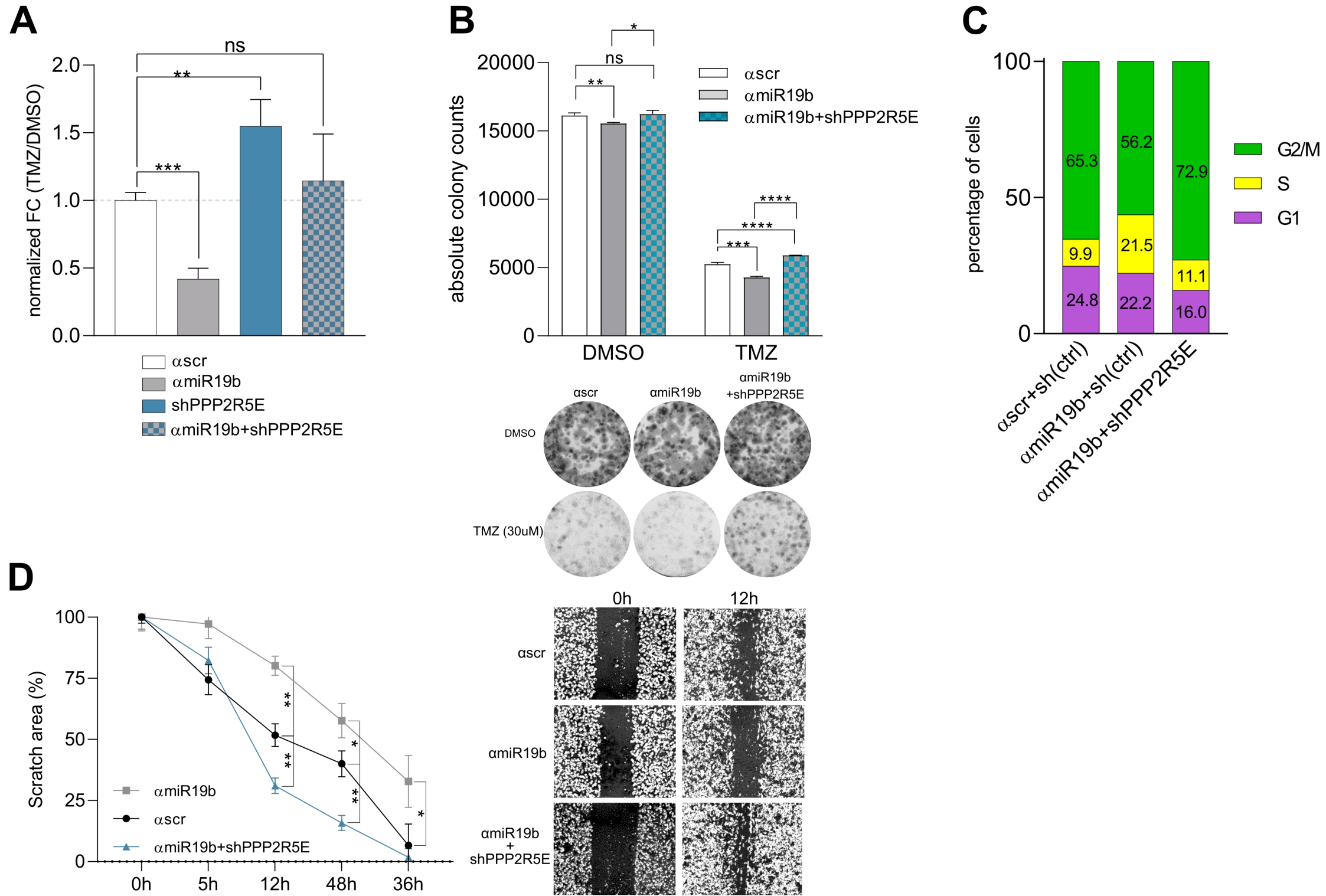
A
normalized FC (TMZ/DMSO)
2.0
1.5
1.0
0.5
0.0
ns
**
***
αscr
αmiR19b
shPPP2R5E
αmiR19b+shPPP2R5E
B
absolute colony counts
20000
15000
10000
5000
0
*
ns
**
****
****
***
αscr
αmiR19b
αmiR19b+shPPP2R5E
DMSO
TMZ
αscr
αmiR19b
αmiR19b +shPPP2R5E
DMSO
TMZ (30uM)
C
percentage of cells
100
50
0
65.3
9.9
24.8
56.2
21.5
22.2
72.9
11.1
16.0
G2/M
S
G1
αscr+sh(ctrl)
αmiR19b+sh(ctrl)
αmiR19b+shPPP2R5E
D
Scratch area (%)
100
75
50
25
0
0h
5h
12h
48h
36h
**
**
*
**
*
αmiR19b
αscr
αmiR19b+shPPP2R5E
0h
12h
αscr
αmiR19b
αmiR19b + shPPP2R5E

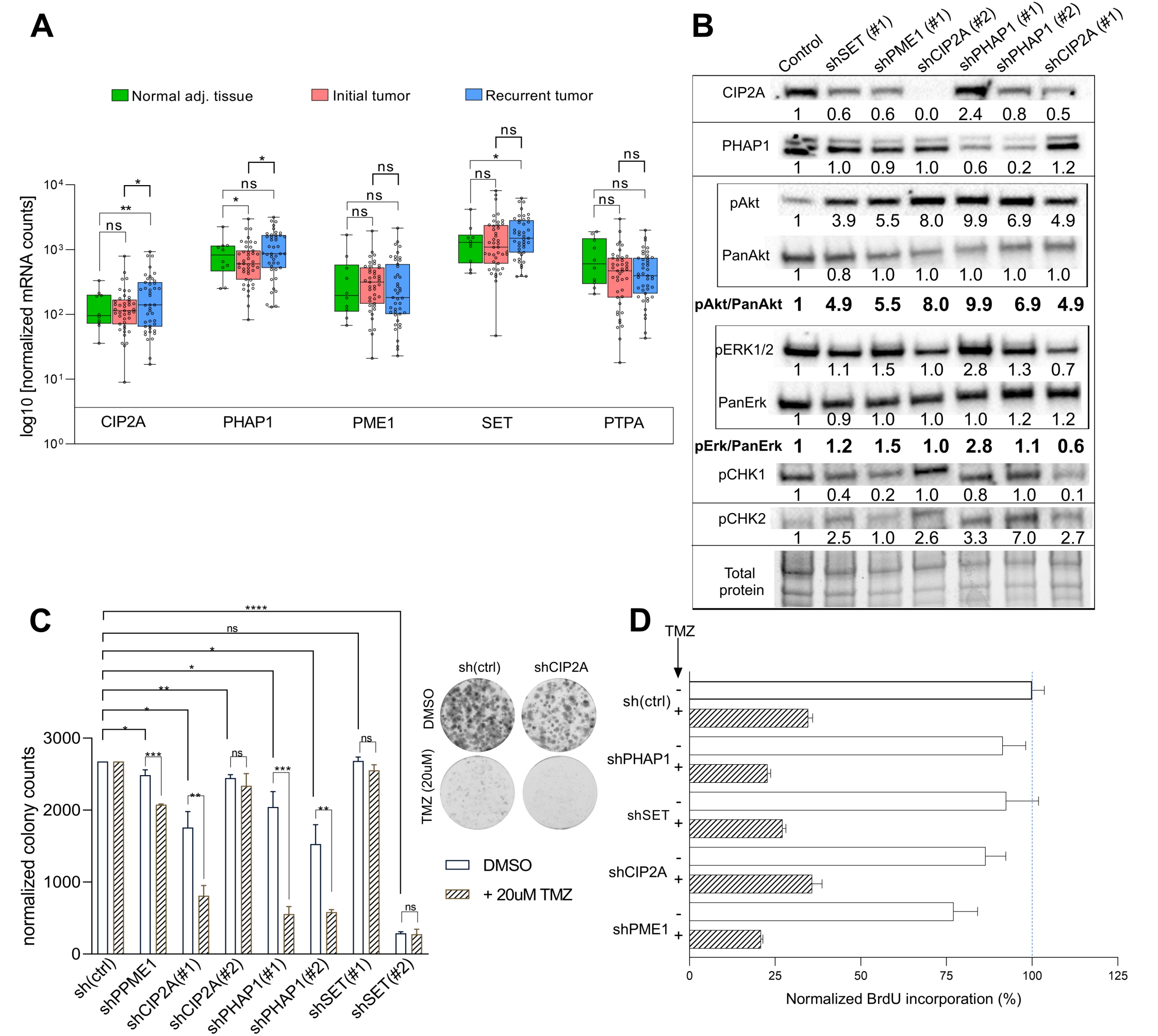
A
Normal adj. tissue
Initial tumor
Recurrent tumor
log10 [normalized mRNA counts]
CIP2A
PHAP1
PME1
SET
PTPA
B
Control
shSET (#1)
shPME1 (#1)
shCIP2A (#2)
shPHAP1 (#1)
shPHAP1 (#2)
shCIP2A (#1)
CIP2A 1 0.6 0.6 0.0 2.4 0.8 0.5
PHAP1 1 1.0 0.9 1.0 0.6 0.2 1.2
pAkt 1 3.9 5.5 8.0 9.9 6.9 4.9
PanAkt 1 0.8 1.0 1.0 1.0 1.0 1.0
pAkt/PanAkt 1 4.9 5.5 8.0 9.9 6.9 4.9
pERK1/2 1 1.1 1.5 1.0 2.8 1.3 0.7
PanErk 1 0.9 1.0 1.0 1.0 1.2 1.2
pErk/PanErk 1 1.2 1.5 1.0 2.8 1.1 0.6
pCHK1 1 0.4 0.2 1.0 0.8 1.0 0.1
pCHK2 1 2.5 1.0 2.6 3.3 7.0 2.7
Total protein
C
normalized colony counts
sh(ctrl)
shPPME1
shCIP2A(#1)
shCIP2A(#2)
shPHAP1(#1)
shPHAP1(#2)
shSET(#1)
shSET(#2)
sh(ctrl)
shCIP2A
DMSO
TMZ (20uM)
DMSO
+ 20uM TMZ
D
TMZ
sh(ctrl)
shPHAP1
shSET
shCIP2A
shPME1
Normalized BrdU incorporation (%)

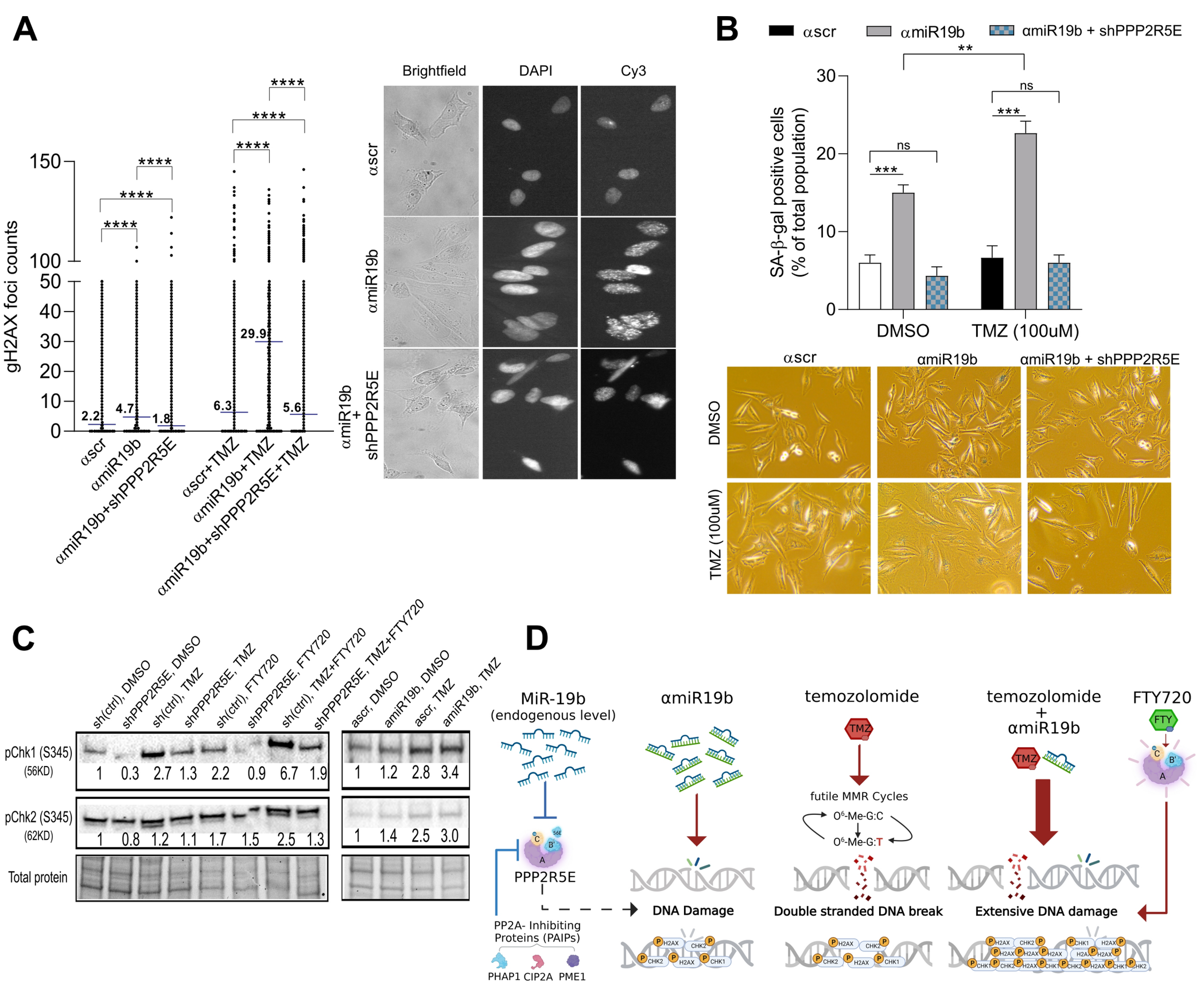
A
gH2AX foci counts
150
100
50
40
30
20
10
0
****
2.2
4.7
1.8
6.3
29.9
5.6
αscr
αmiR19b
αmiR19b+shPPP2R5E
αscr+TMZ
αmiR19b+TMZ
αmiR19b+shPPP2R5E+TMZ
Brightfield
DAPI
Cy3
αmiR19b + shPPP2R5E
B
αscr
αmiR19b
αmiR19b + shPPP2R5E
SA-β-gal positive cells (% of total population)
**
ns
***
DMSO
TMZ (100uM)
C
sh(ctrl), DMSO
shPPP2R5E, DMSO
sh(ctrl), TMZ
shPPP2R5E, TMZ
sh(ctrl), FTY720
shPPP2R5E, FTY720
sh(ctrl), TMZ+FTY720
shPPP2R5E, TMZ+FTY720
ascr, DMSO
amiR19b, DMSO
ascr, TMZ
amiR19b, TMZ
pChk1 (S345) (56KD)
1 0.3 2.7 1.3 2.2 0.9 6.7 1.9
1 1.2 2.8 3.4
pChk2 (S345) (62KD)
1 0.8 1.2 1.1 1.7 1.5 2.5 1.3
1 1.4 2.5 3.0
Total protein
D
MiR-19b (endogenous level)
αmiR19b
temozolomide
temozolomide + αmiR19b
FTY720
TMZ
FTY
futile MMR Cycles
O6-Me-G:C
O6-Me-G:T
PPP2R5E
DNA Damage
Double stranded DNA break
Extensive DNA damage
PP2A- Inhibiting Proteins (PAIPs)
PHAP1 CIP2A PME1

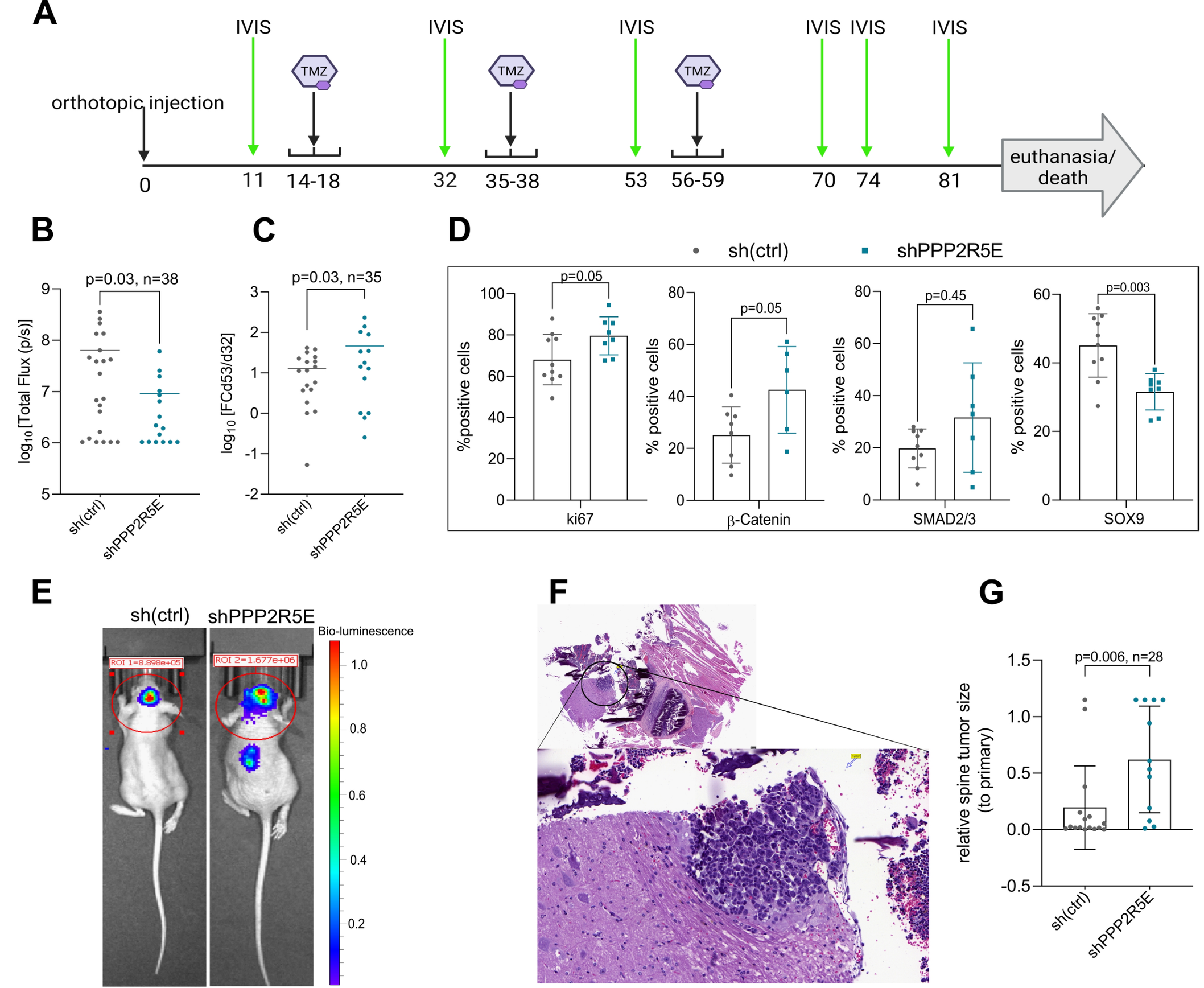
A
IVIS
IVIS
IVIS
IVIS
IVIS
IVIS
TMZ
TMZ
TMZ
orthotopic injection
0
11
14-18
32
35-38
53
56-59
70
74
81
euthanasia/ death
B
p=0.03, n=38
log10[Total Flux (p/s)]
sh(ctrl)
shPPP2R5E
C
p=0.03, n=35
log10 [FCd53/d32]
sh(ctrl)
shPPP2R5E
D
sh(ctrl)
shPPP2R5E
p=0.05
%positive cells
ki67
p=0.05
% positive cells
β-Catenin
p=0.45
% positive cells
SMAD2/3
p=0.003
% positive cells
SOX9
E
sh(ctrl)
shPPP2R5E
Bio-luminescence
ROI 1=8.898e+05
ROI 2=1.677e+06
F
G
p=0.006, n=28
relative spine tumor size (to primary)
sh(ctrl)
shPPP2R5E